Nano Research
2021, 14(4): 1087–1094

ISSN 1998-0124 CN 11-5974/O4
https://doi.org/10.1007/s12274-020-3153-6

Research Article

In situ self-assembly of near-infrared-emitting gold nanoparticles into body-clearable 1D nanostructures with rapid lysosome escape and fast cellular excretion

Kui He, Jiayi Zhu, Lingshan Gong, Yue Tan, Huarui Chen, Huarun Liang, Baihao Huang, and Jinbin Liu (✉)

Key Laboratory of Functional Molecular Engineering of Guangdong Province, School of Chemistry and Chemical Engineering, South China University of Technology, Guangzhou 510640, China

Received: 27 July 2020 / **Revised:** 29 September 2020 / **Accepted:** 1 October 2020

ABSTRACT

The integration of strong near-infrared (NIR) emission, rapid lysosome escape, fast cellular excretion, and efficient total body clearance is highly desired for nanoparticles (NPs) to achieve synergistic functions in both molecular imaging and delivery. Herein, using a well-designed cyclopeptide (CP) that can spontaneously assemble into controllable nanofibers as template, a facile strategy is reported for *in situ* self-assembly of NIR-emitting gold NPs (AuNPs) into ordered and well-controlled one-dimensional (1D) nanostructures (AuNPs@CP) with greatly enhanced NIR emission (~ 6 fold). Comparing with the unassembled AuNPs, the AuNPs@CP are observed to enter living cells through endocytosis, escape from lysosome rapidly, and excrete the cell fast, which shows high gene transfection efficiencies in construction of cell line with ~ 7.5-fold overexpression of p53 protein. Furthermore, the AuNPs@CP exhibit high *in vivo* diffusibility and total body clearance efficiency with minimized healthy organ retention, which are also demonstrated to be good nanovectors for plasmid complementary deoxyribonucleic acid 3.1 (pcDNA3.1)(+)-internal ribosome entry site (IRES)-green fluorescent protein (GFP)-p53 plasmid with efficient *p53* gene over-expression in tumor site. This facile *in situ* strategy in fabricating highly luminescent 1D nanostructures provides a promising approach toward future translatable multifunctional nanostructures for delivering, tracking, and therapy.

KEYWORDS

luminescent gold nanoparticle, self-assembly, intracellular imaging, body clearance, gene delivery

1 Introduction

Ultrasmall luminescent gold nanoparticles (AuNPs, d < 3 nm) with unique optical properties, low toxicity, long blood circulation and high metabolic clearance [1–4], have received immense interest in biosensing, bioimaging and therapy [5–9]. Recently, the ultrasmall visible-emitting AuNPs after functionalization (e.g., oligoarginine) were demonstrated to be nanovectors for deoxyribonucleic acid (DNA)/small interfering ribonucleic acid (siRNA)/drug delivery [10–12]. Furthermore, self-assembly of the pre-synthesized ultrasmall AuNPs using cationic polymer as a template was shown as a promising strategy for enhancements both in emission and drug delivery efficiencies [13]. Although many beneficial advantages have been achieved using ultrasmall AuNPs as delivery vectors, including good biocompatibility, low cytotoxicity, and high cellular internalization, the self-assembled nanostructures are typically internalized via endocytosis pathways, raising another challenge in the endo/lysosomal trapping and degradation [14, 15]. Therefore, the development of self-assembled AuNPs to facilitate the endo/lysosomal escape for improved delivery efficiency is highly desirable. In addition, the hard degradation or low body clearance of the typical nanostructures also cause the anxiety of biosafety problems, impeding the future clinical translation. Since the emission of the reported AuNPs was in the visible range (e.g., ~ 600 nm) that could be easily interfered by the bioluminescence background from cellular environment, how to achieve accurate and body-clearable self-assembled nanostructures with emission in the near-infrared (NIR) range for integration of subcellular tracking and delivery in a facile *in situ* strategy remains unsolved.

Synthetic peptides with advantages of biocompatibility, multifunctionality, and biodegradability are perfect building blocks for self-assembling NPs into biological systems for drug delivery, cancer therapy, and regenerative medicine [16, 17]. Peptide self-assembly has achieved remarkable advances, and several studies have concentrated on peptide molecular design and related self-assembled nanostructures, which were obtained through noncovalent interactions including hydrogen bonding, hydrophobic interactions, and π–π stacking interactions [18, 19]. For example, the self-assembled tryptophan-phenylalanine dipeptide NPs with diameter of ~ 160 nm, could shift the peptides' intrinsic emission signal from ultraviolet to visible range for monitoring drug release [20]; the polymer-beclin-1 (P-Bec1)-based self-assembled NPs with diameter of ~ 32 nm at pH 7.4, showed effectively induced autophagy and inhibited tumor growth [21]. However, although various functional nanostructures from synthetic peptides were constructed [22, 23], the ability of peptides in the *in situ* self-assembly of ultrasmall NIR-emitting AuNPs is still unknown, which is of great

Address correspondence to cejbliu@scut.edu.cn

importance in the emergence of multifunctional nanostructures for various biomedical applications.

Herein, we designed a cyclopeptide (CP) that spontaneously assembled into nanofibers with controllable lengths in solution under different pH conditions, which could be utilized for *in situ* assembly of NIR-emitting AuNPs into ordered and well-controlled one-dimensional (1D) nanostructures (AuNPs@CP). The fabricated AuNPs@CP showed a maximum emission at 810 nm with quantum yield (QY) as high as 5.9%, significantly higher than most of the previously reported NIR-emitting AuNPs (~ 1%) [24, 25]. Using the enhanced NIR emission, we observed that the AuNPs@CP entered cell through endocytosis but escaped from lysosome rapidly, significantly different from the unassembled ones in either cellular endocytosis or efflux, resulting in high capability in construction of cell line with ~ 7.5-fold overexpression of p53 protein as compared to the wild-type HeLa cell. Both NIR fluorescence imaging and biodistribution investigations revealed that the unique 1D AuNPs@CP nanostructures showed high diffusibility after intratumoral (i.t.) injection and could be eliminated from the body via both renal and hepatic metabolic pathways with minimized accumulation in healthy organs. The 1D AuNPs@CP nanostructures were then demonstrated as robust nanovectors for plasmid complementary deoxyribonucleic acid 3.1 (pcDNA3.1)(+)-internal ribosome entry site (IRES)-green fluorescent protein (GFP)-p53 to show overexpressed p53 protein in MDA-MB-231 tumor. Together with the enhanced NIR emission, the rapid lysosome escape, and cellular efflux, high *in vivo* diffusibility and the unique body clearance properties make this 1D nanostructures promising for practical use in both tracking and cancer therapy.

2 Results and discussion

2.1 Synthesis and characterization of 1D NIR-emitting AuNPs@CP nanostructures

The sequence of the designed CP was cyclo-(Ala-Arg-Ala-Arg-Ala-Arg-Ala-Asp)-aminocaproic-Cys (Fig. S1 in the Electronic Supplementary Material (ESM)). The arginines were used to form bidentate hydrogen bonds with anionic groups in both DNA and cell membranes, and the cysteine on the terminal of branched chain was selected to provide binding site for *in situ* self-assembly of ultrasmall AuNPs. The hydrogen-bond donors and acceptors were complementary in each side of the CP to facilitate formation of inherent self-assembled nanofibers (Fig. 1(a)) [26, 27]. As expected, the CP could easily self-assemble into nanofibers with pH-dependent lengths visualized in the atomic force microscopic (AFM) images. Upon decreasing pH value to 3.0, the CP formed stable nanofiber with micro-scale length. However, it was difficult to form stable nanostructures under strong alkaline conditions (e.g., pH 11) due to strong intermolecular resistance among CP molecules (Fig. 1(b)). Therefore, the inherent self-assembled nanofibers exhibited uniform lengths of ~ 300–700 nm with an average height of ~ 6.5 Å under neutral or weak alkaline conditions (e.g., pH 6.5–10.0), which were selected as templates for the following *in situ* fabrication investigations.

The luminescent AuNPs@CP was then *in situ* fabricated using the inherent CP nanofiber as template under weak alkaline conditions in the presence of $HAuCl_4$ and glutathione (GSH) at 95 °C (Fig. 2(a), Fig. S2 in the ESM). The AuNPs@CP exhibited NIR emission with a maximum at 810 nm (Fig. 2(b)), and the QY was measured to be 5.9% in water using fluorescein as reference, which was ~ 6 times higher than those of the previously reported NIR-emitting AuNPs (~ 1%) [24, 25]. The mixed valence of Au(0) and Au(I) was achieved with Au(I) species of ~ 36.4% (Fig. S3 in the ESM), consistent with most of the reported NIR-emitting AuNPs [24, 25], suggesting the self-assembly induced emission enhancement of the AuNPs on the CP nanofiber. The ultraviolet (UV)–visible (vis) absorption spectrum showed abroad absorption in the range of 200–400 nm, but no characteristic surface plasmonic band around 520 nm (Fig. 2(b)), indicating the generation of ultrasmall AuNPs on the CP nanofiber and no formation of larger plasmonic AuNPs during the *in situ* fabrication process. The fibrous structure of AuNPs@CP was clearly visible in the transmission electron microscopic (TEM) images (Fig. 2(c), Fig. S4(a) in the ESM), and the AuNPs with size of 1.8 ± 0.3 nm were homogeneously distributed on CP template. The lengths of AuNPs@CP were measured to be ~ 600 nm in the scanning electron microscopic (SEM) image (Fig. 2(d), Fig. S4(b) in the ESM), and a height increase of ~ 1.1 nm as compared to the inherent CP nanofiber in the AFM images (Fig. 2(e), Figs. S4(c) and S4(d) in the ESM), further confirming the generation of AuNPs on the fibrous CP template. The prepared AuNPs@CP integrated the features of uniform lengths, ordered, and well-controlled morphology due to the *in situ* strategy of facile preparation and good controllability, which allowed Au atoms to fully combine with the sulfhydryl group on the CP to form 1D nanostructures. The elemental analysis of AuNPs@CP revealed the ratio of CP to GSH was 1:19.5, which was consistent with the added dosage ratio between CP and GSH in the reaction process (Fig. S5 in the ESM). Stability is an important factor to evaluate

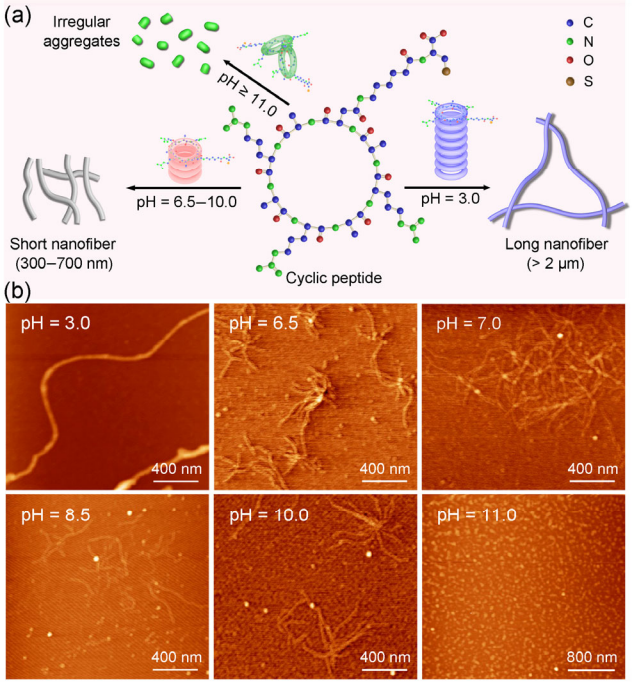

Figure 1 The self-assembled nanofibers of CP with pH-dependent lengths. (a) Schematic diagram of the spontaneous self-assembly of CP under different pH conditions. The CP interacted through an extensive network of hydrogen bonds to form a stable nanofiber structure under different conditions. (b) AFM images of the inherent self-assembled CP nanostructures at different pH values: 3.0, 6.5, 7.0, 8.5, 10.0, and 11.0. These results indicated that the nanofiber exhibited uniform lengths about 300–700 nm at neutral or alkaline pH values, which was attributed to the hydrogen-bonding interactions between the amide groups and the carbonyl group of amino acids on the ring. Upon decreasing pH value to 3.0, the CP formed stable nanofiber with micro-scale length (> 2 μm). However, it was difficult to form stable nanostructures under strong alkaline conditions (e.g., pH > 11.0) due to strong intermolecular resistance among the CP molecules.

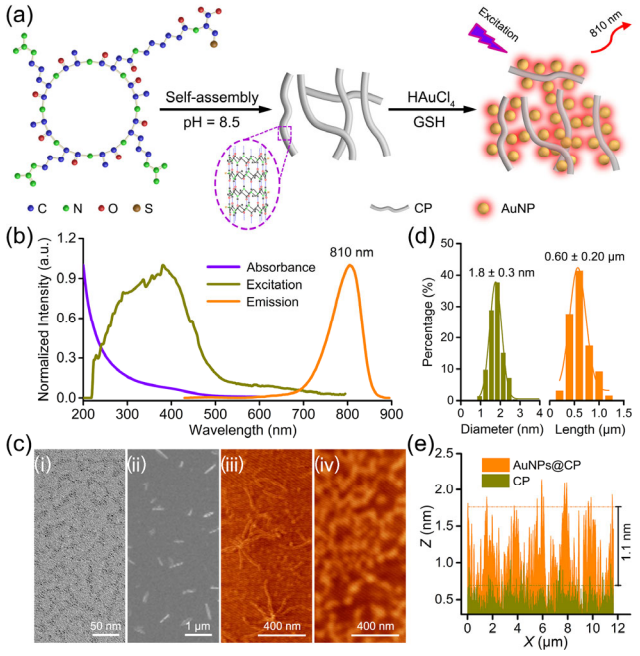

Figure 2 Preparation and characterization of *in situ* self-assembled NIR-emitting AuNPs@CP. (a) Schematic illustration of the self-assembled CP and the *in situ* self-assembly process of AuNPs@CP. (b) Absorption, excitation, and emission spectra of AuNPs@CP. (c) TEM (i), SEM (ii), and AFM (iv) images of AuNPs@CP. AFM images of CP before (iii) and after (iv) self-assembly of AuNPs were compared. (d) Size analysis of AuNPs on the nanofibers and lengths analysis of AuNPs@CP calculated from corresponding TEM and SEM images. (e) Height profile analysis of CP and AuNPs@CP.

the functions of self-assembled nanostructures for further bioapplications [28, 29]. The emission of AuNPs@CP was quite stable in physiological mediums (Fig. S6 in the ESM), as well as against high ionic strength and pH changes (Fig. S7 in the ESM).

2.2 Cellular endocytosis pathways and co-localization analysis

The intrinsic NIR emission of AuNPs@CP could provide a feasible way for further imaging the pathways of entering cells and ultimate whereabouts, which was critical for practical future applications [30, 31]. Since endocytosis via lysosome transportation is a typical entry pathway for typical NPs [32, 33], the pathway of AuNPs@CP was investigated through imaging the co-localization of AuNPs@CP and lysosome inside HeLa cells at different incubation time points. The HeLa cells were firstly transfected using Lysosomes-GFP Bac Mam 1.0 kits for Lamp1 (lysosome marker) labeling, whose endosomal structures were stained with green fluorescence with wavelength far away from the NIR emissions of AuNPs@CP to minimize the color interferences. The gradual decrease of the colocalization between AuNPs@CP and lysosome after incubation from 1 to 12 h with statistical colocalization Pearson's correlation coefficient (R_r) [34] decreased from 0.62 to 0.37 (Figs. 3(a) and 3(c)), distinct from the glutathione coated AuNPs (GS-AuNPs) with a similar R_r (~ 0.58), suggested that AuNPs@CP firstly entered lysosome through endocytosis but escaped from lysosome rapidly. However, after removal of the medium containing the NPs, the GS-AuNPs showed an even increased R_r of 0.64 after incubation for 12 h in GS-AuNPs free medium, indicating GS-AuNPs might be trapped in lysosomes (Figs. 3(b) and 3(c)). The significant differences in the cellular pathways between AuNPs@CP and GS-AuNPs further confirmed that AuNPs@CP with self-assembled fibrous nanostructure showed the unique capability of rapid cellular membrane fusion and lysosome escaping.

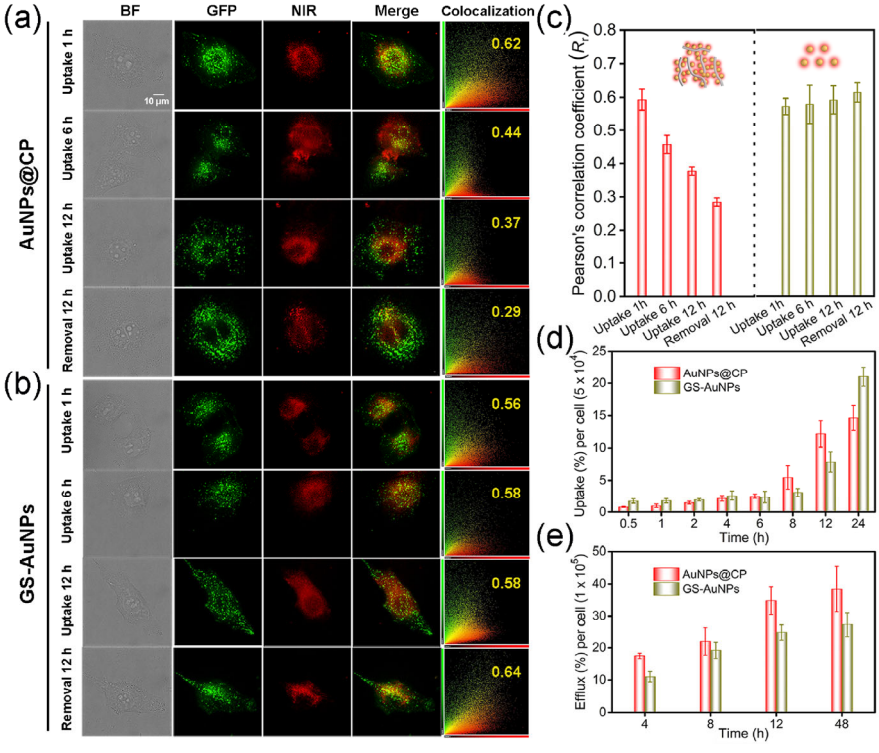

Figure 3 Cell imaging and co-localization analysis. (a) Colocalization analysis between AuNPs@CP (red channel) and GFP-labeled lysosomes (green channel). The HeLa cells were imaged after incubation with AuNPs@CP for different time points (1, 6, 12 h, from first to third row). Pearson's correlation coefficients were displayed in yellow. (b) Colocalization analysis between GS-AuNPs (red channel) and GFP-labeled lysosomes (green channel). The GS-AuNPs were used as control. (c) Statistical analysis of colocalization coefficients (AuNPs@CP, left) and (GS-AuNPs, right) from HeLa cells in different time. (d) Cellular uptake efficiencies of AuNPs@CP and GS-AuNPs at different incubation time. (e) Efflux percentages of AuNPs@CP released at different incubation time.

The efficiencies of cellular endocytosis and efflux of AuNPs@CP were subsequently analyzed using inductive coupling plasma mass spectrometry (ICP-MS). The results indicated that the internalization amount of both AuNPs@CP and GS-AuNPs increased with prolonged incubation time (Fig. 3(d)). Interestingly, the internalization amount of AuNPs@CP by HeLa cells was 1.4-fold more than that of the GS-AuNPs after 12-h incubation, but the internalization amount of AuNPs@CP was obviously less than that of GS-AuNPs at 24 h. The reasonable explanation might be the different pathways to enter and leave cells. Then several inhibitors including amiloride, chlorpromazine, sodium azide (NaN_3), and methyl-β-cyclodextrin (m-βCD) were introduced to evaluate their inhibiting effects to understand the internalization mechanism of AuNPs@CP and GS-AuNPs, respectively [35]. These results showed that cellular uptake of AuNPs@CP was affected by both NaN_3 and m-βCD (Fig. S8(b) in the ESM), which reduced the amount of cholesterol on the membrane and inhibited the membrane cellar mediated endocytosis [36, 37]. This phenomenon showed the design of CP with 4 alanines could make it self-assembly to form nanofibers with hydrophobic ends, which might interact with cholesterol, phospholipids, and other hydrophobic substances on the membrane for cellular endocytosis (Fig. S8(a) in the ESM). Nevertheless, the cellular uptake of GS-AuNPs was mainly affected by amiloride, which inhibited the endocytosis pathway of the giant pinocytosis, as well as NaN_3 (Fig. S8(c) in the ESM), which blocked the transfer of electron transport chain, and thereby blocked the energy metabolism [38, 39]. We also tested the cellular efflux kinetics of AuNPs@CP and GS-AuNPs at different time points after 12-h uptake (Fig. 3(e)). These results demonstrated that the removal rate of AuNPs@CP was obviously faster than that of GS-AuNPs and the efflux efficiency of AuNPs@CP was approximately 40% after 48 h, which was consistent with the results of cell pathways studies. Therefore, the *in situ* fabricated AuNPs@CP were not only able to possess the capability of intracellular translocation, but also could be rapidly excreted from the cells, holding great promising in visualization therapy.

2.3 *In vitro* gene transfection and construction of *p53* overexpressed cell lines

To evaluate the loading and transfection capacity of 1D nanostructures, the GFP plasmid, a representative reporter gene plasmid in transfection experiments, was mixed with AuNPs@CP to incubate with HeLa cells for 12 h without other assistant molecules such as lipids or cationic polymers, which were often used as artificial transfection vectors to ensure gene transfection. The expression of GFP inside the HeLa cells demonstrated that AuNPs@CP successfully transported the GFP plasmid into HeLa cells (Fig. S9 in the ESM). The above results clearly demonstrated that luminescent AuNPs@CP as novel delivery vectors possessed transfection capability due to the specific 1D nanostructures with both high plasmid DNA loading and cellular internalization abilities [40].

In order to further assess the delivery efficiency, a plasmid DNA (pDNA) with overexpression of *p53* gene (a vitally important tumor suppressor gene) [41, 42] was designed via inserting *p53* gene regulatory sequence into pcDNA3.1(+)-IRES-GFP plasmid vector to construct the cell lines overexpressed with *p53* gene (Fig. S10(a) in the ESM). The emission of AuNPs@CP did not change obviously after mixing with pDNA, but the absorbance enhanced significantly (Figs. S10(b) and S10(c) in the ESM), indicating the conjugation between pDNA and AuNPs@CP. The formed nanocomplexes between pDNA and AuNPs@CP (AuNPs@CP-pDNA) were also observed in both AFM (Figs. S10(d) and S10(e) in the ESM) and TEM images (Fig. S10(f) in the ESM), further confirming the strong interaction between pDNA and AuNPs@CP, which could facilitate gene transfection for loading pDNA into cells. Using a commercially available vector polyethyleneimine (PEI) as control [43], we then tested the transfection properties of AuNPs@CP in HeLa Cells. The HeLa cells were highly bright expressed with GFP as observed in the fluorescent microscopic images after pcDNA3.1(+)-IRES-GFP-p53 plasmid was transfected using AuNPs@CP (Figs. 4(a) and 4(b), detailed pDNA transfection and GFP expression detection were shown in the methods section). After statistic calculation of the number ratio between the cells with GFP fluorescence and the total cells, the transfection efficacy of AuNPs@CP was ~ 60.4%, higher than that of the PEI (~ 55.7%) or CP fibrous template (~ 36.7%) (Fig. 4(c)). The viabilities of HeLa cells treated with AuNPs@CP at different concentrations were evaluated using cell counting kit-8 (CCK-8) assays, which showed negligible cytotoxicity (Fig. 4(d)), in sharp contrast to those of the PEI with significant nanotoxicities even at low concentrations (Fig. 4(e)). Furthermore, western blotting analysis of p53 protein levels in wild-type and the HeLa cells transferred by vectors including GS-AuNPs, CP, PEI, and AuNPs@CP. The gray value of the bands represented the expression content of p53 protein and the internal control protein glyceraldehyde-3-phospheate dehydrogenase (GAPDH), respectively. As shown in Fig. 4(f), the cell line after transfection with GS-AuNPs and CP exhibited ~ 2.0-fold and ~ 4.7-fold overexpression of p53 protein as compared to the wild-type HeLa cells, respectively. The PEI group showed high expression of p53 protein induced by DNA damage due to the high toxicity of PEI in current concentration [44, 45]. In addition, the cell line after transfection using AuNPs@CP exhibited ~ 7.5-fold overexpression of p53 protein as compared to the wild-type HeLa cells, further demonstrating that AuNPs@CP were excellent nanovectors for *in vitro* gene transfection.

2.4 *In vivo* NIR imaging and biodistribution of AuNPs@CP-pDNA

The diffusibility in tumor site and metabolic pathway of the AuNPs@CP after loading pDNA were then investigated by collecting the time-dependent fluorescence images of MDA-MB-231 tumor-bearing nude mice after i.t. injection (Fig. 5(a)). The NIR emission signals in the tumor site decreased monotonously at different post injection (p.i.) time points (Figs. 5(b) and 5(c)), indicating the high diffusibility of the 1D AuNPs@CP in the tumor site. In sharp contrast to the tumor site, the bladder was readily observed with increased NIR signals from 10 min to 1.5 h p.i. (Fig. 5(b)), demonstrating the renal clearance of the AuNPs@CP. To acquire a more quantitative understanding of the *in vivo* behavior, we studied the biodistribution of the AuNPs@CP-pDNA after i.t. injection at 72 h p.i. (Fig. 5(d)). The tumor retention was measured to be 21.8% injection dose (ID)/g. The major organs (e.g., heart, liver, spleen, and lung) showed minimized retention (less than ~ 5% ID/g), except the kidney with a high distribution of ~ 20.7% ID/g, consistent with renal clearance observed from the imaging analysis (Fig. 5(b)). In addition, the urine and feces were determined to be (35.2 ± 2.6)% ID and (15.3 ± 7.6)% ID, respectively, which further demonstrated that the body clearance of AuNPs@CP-pDNA through both renal and hepatic pathways. The 1D AuNPs@CP disassembled into individual AuNPs after body circulation as observed from the TEM images of collected urine (Fig. S11 in the ESM). To evaluate the gene delivery efficiency of AuNPs@CP, the tumors after i.t. injection at 72 h p.i. were separated from the nude mice, followed by measuring

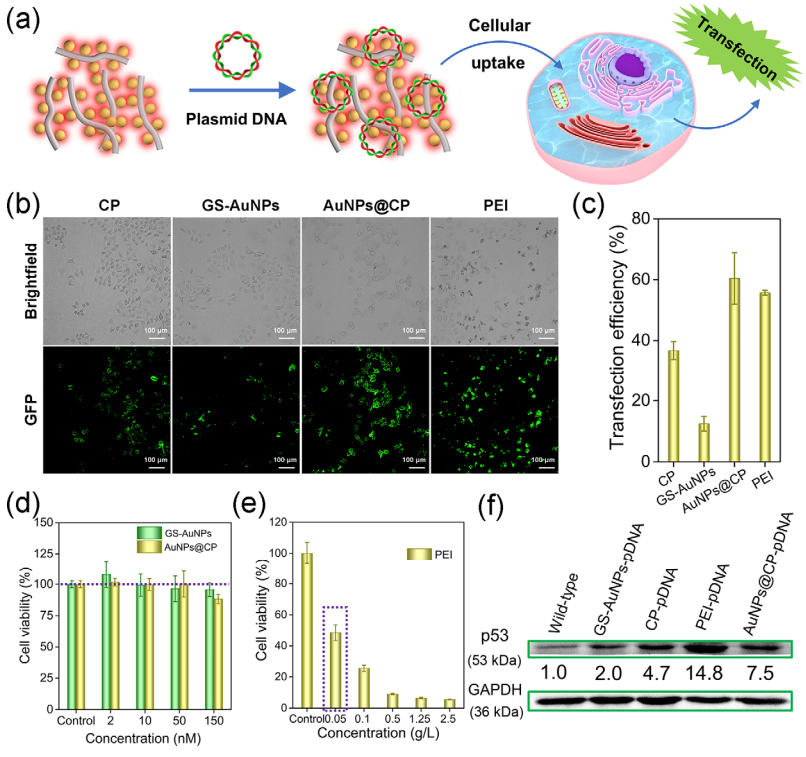

Figure 4 Gene transfection and construction of overexpressed cell lines. (a) Schematic presentation of strong interaction between plasmid DNA and AuNPs@CP, which loaded plasmid into cells to facilitate gene transfection. (b) The brightfield and fluorescent images of HeLa cells after transfection of pcDNA3.1(+)-IRES-GFP-p53 plasmid using different vectors. (c) Transfection efficiencies of the vectors. (d) and (e) Cell viabilities of HeLa Cells after treated with different vectors at different concentrations using CCK-8 assay. (f) Expression level of p53 protein in HeLa cells evaluated by western blotting.

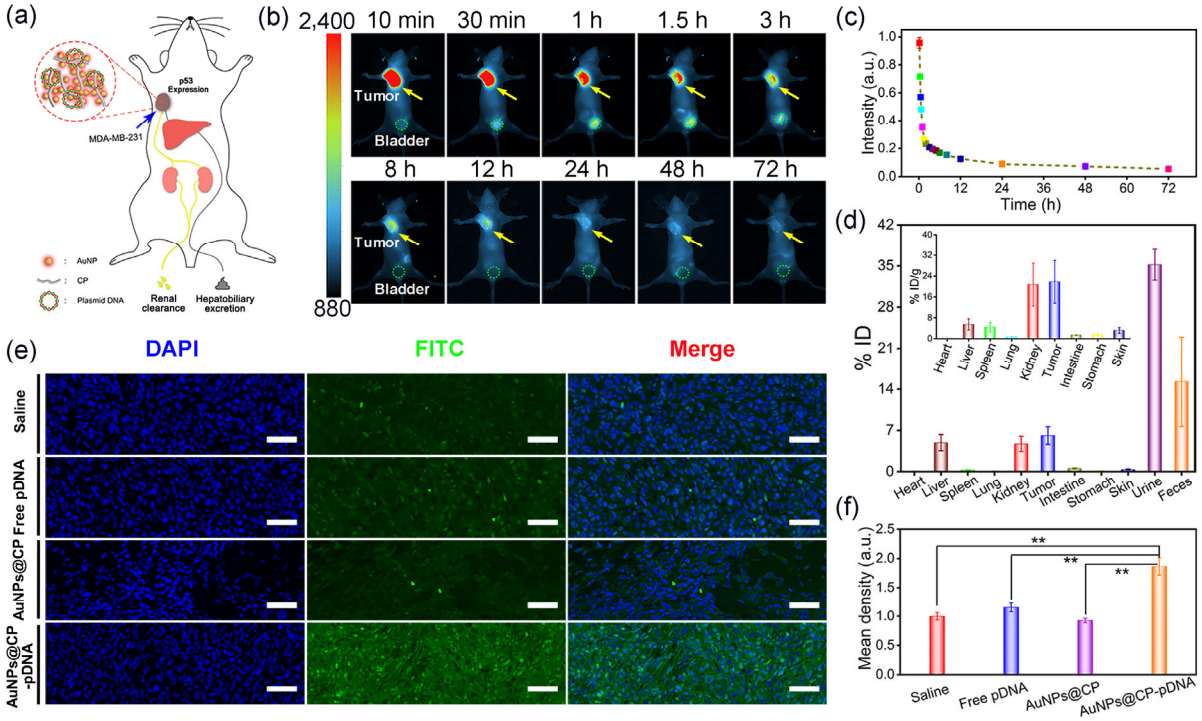

Figure 5 Diffusibility, metabolic pathway, and *in vivo* transfection analysis via i.t. administration. (a) Scheme of the i.t. injection. (b) *In vivo* imaging of the MDA-MB-231 tumor-bearing nude mice after i.t. injection of AuNPs@CP-pDNA. (c) Fluorescent signal statistics obtained from the tumor site. (d) Biodistribution of AuNPs@CP-pDNA at 72 h p.i. (e) Immunofluorescence images of p53 protein (green) in the subcutaneous tumors after *in vivo* transfection. The cell nuclei were stained with DAPI; blue. Scale bars: 50 μm. (f) The overexpression of p53 protein in the MDA-MB-231 tumors after *in vivo* transfection. Significant differences were obtained from the controls, $^{*}0.01 < P < 0.05$, $^{**}P < 0.01$; Student's *t*-test.

the expression level of i.t. p53 protein with a typical immunofluorescence (IF) staining method [46]. The group i.t. injected with AuNPs@CP-pDNA showed a ~ 1.9-fold density increase of i.t. p53 protein as compared to the group of saline, significantly higher than that of the free pDNA or single AuNPs@CP treatment (Figs. 5(e) and 5(f)). By taking the advantages of high body clearance of the 1D nanovectors, the main organs after i.t. injection showed no obvious histological

changes comparing with the control group i.t. injected with saline or free pDNA alone (Fig. S12 in the ESM). The results revealed that the 1D AuNPs@CP had negligible toxicity on the main organs of the mice and the 1D nanostructures of NIR-emitting AuNPs@CP would be excellent nanovectors for *in vivo* gene therapy.

3 Conclusions

In summary, we have successfully achieved *in situ* self-assembly of NIR-emitting AuNPs@CP with 1D nanostructure using a well-designed CP nanofiber as template. The CP containing 3 arginines and 4 alanines in a cyclic ring and 1 cysteine on the terminal of branched chain could form inherent nanofibers with controllable lengths in solution under different pH conditions, which served as a good template to *in situ* self-assemble 810 nm-emitting AuNPs with both well-defined 1D nanostructures and enhanced emission (QY, 5.9%). Taking advantages of the intrinsic NIR emissions for intracellular imaging, it was revealed that the self-assembled 1D nanostructure of AuNPs@CP showed unique capability of rapid cellular membrane fusion, efficient lysosome escape, and fast cellular efflux as compared to the unassembled ones, resulting in high capability in construction of cell line with 7.5-fold overexpression of p53 protein comparing to the wild-type HeLa cell. Both NIR fluorescence imaging and biodistribution investigations revealed that the novel 1D AuNPs@CP nanostructures after i.t. injection showed high diffusibility and could be effectively eliminated from the body via both renal and hepatic metabolic pathways with extremely low retention in the healthy organs. Furthermore, the enhancement of *p53* gene overexpression in tumor site was also demonstrated using the 1D AuNPs@CP as featured nanovectors. These findings establish this *in situ* strategy as a facile and feasible method for self-assembly of highly luminescent metal NP-based 1D nanostructures for gene delivery. Considering the high penetration depth of the second near-infrared (NIR-II, 1000–1700 nm) window, this *in situ* strategy is highly expected to be used for obtaining NIR-II emitting 1 D nanostructures toward precise cancer diagnosis and therapy in the future.

4 Experimental

4.1 *In situ* self-assembly of luminescent AuNPs@CP using CP as template

The luminescent AuNPs@CP was *in situ* fabricated using inherent formed CP nanofiber as template under weak alkaline condition in the presence of $HAuCl_4$ and GSH with the molar ratio of CP to GSH of 1:20 according to the method that we used to create GS-AuNPs. Typically, into a 5-mL reaction tube were added 84 μL of $HAuCl_4$ (73.0 mM), 272 μL of NaOH (0.1 M), 51.2 μL of CP (6.0 mM), and 256 μL of GSH (24.0 mM) were mixed thoroughly before ultrapure water was supplemented to a total volume of 2.0 mL. The mixed solution was stirred vigorously in oil bath at 95 °C for 12 h, and the final color of the solution was pale brown, indicating the formation of AuNPs@CP. The pH of the above solution maintained ~ 8.5–10.0 using additional NaOH (0.1 M) during all the reaction process. After that, the resulting solution was purified by dialysis (3.5 kDa) in water, followed by the ultrafiltration with 10 kDa molecular weight cut-off (MWCO) membrane. As control, the nonassembled GSH coated AuNPs (GS-AuNPs) was synthesized according to our previously reported method with a slight modification that the pH of the reaction was changed to ~ 8.5–10.0. The purified AuNPs@CP or GS-AuNPs solution was stored at 4 °C before further use.

4.2 Cellular imaging and co-localization analysis

HeLa cells with ~ 60%–70% density were seeded into dish and incubated at 37 °C in Dulbecco's modified Eagle's medium (DMEM) supplemented with 10% fetal bovine serum (FBS) and 1% penicillin-streptomycin (PS, culture medium) for 24 h to allow the cells to adhere to the surface. Then HeLa cells were transfected by using Lysosomes-GFP BacMam 1.0 kits to obtain the cells with Lamp1 labeling. Afterwards, the obtained cells were seeded into confocal dish at a density of 2×10^3 cells and maintained in culture medium for 24 h to grow well. Finally, after removal of the medium, the cells were incubated in DMEM containing GS-AuNPs (43 nM) and AuNPs@CP (43 nM) at different time points, respectively, to observe the pathways of entering and leaving cells. Endosomal structures were stained with GFP. The AuNPs@CP or GS-AuNPs showed NIR emission for the co-localization experiments, which were performed on a fully-motorized inverted microscope system (Olympus IX83-DSU, Japan, equipped with a spinning disk confocal technology) assembled with both Photometrics EMCCD (Evolve 512 Delta) and Retiga R1 CCD, through a 100X oil-immersion objective under Xe-lamp excitation (green channel for lysosomes-GFP imaging, ex: 460–480 nm, em: 495–540 nm; and red channel for 810 nm-emitting imaging, ex: 355–375 nm, em: 765–855 nm).

4.3 *In vitro* transfection

HeLa cells with ~ 40%–50% density were seeded into confocal dish and maintained in culture medium for 24 h to allow the cells to adhere to the surface. The vectors including CP (15 μM), GS-AuNPs (43 nM), AuNPs@CP (43 nM) and PEI (0.05 g/L) were mixed in Opti-MEM with 2 μg plasmid DNA at room temperature for 30 min, respectively. Then the obtained solutions were transfected into HeLa cells and incubated for 12 h, respectively. Finally, the medium was removed completely and culture medium was added to generate the expression of GFP. The expression of GFP was observed by a fully-motorized inverted microscope system.

4.4 Animal studies

The balb/c nude mice (4 weeks, female) were obtained from the Laboratory Animal Center of Guangdong Province (Guangdong, China), and housed in the Laboratory Animal Center of South China Agricultural University with an adaption time of at least 7 days before the beginning of the experiments. All procedures for animal studies were strictly in compliance with the guidelines for the care and use of laboratory animals, as well as in accordance with the regulations on the management of laboratory animals of China and the Regulations on the Administration of Laboratory Animals of Guangdong Province. MDA-MB-231 tumor cells (2×10^6 cells per mice) were injected subcutaneously into the right site of breast of female nude mice. With the growth of tumor size ~ 50–80 mm^3 in diameter, the mice were used for the following experiments.

4.5 *In vivo* NIR imaging

The AuNPs@CP-pDNA (80 μL, 1.3 μM of AuNPs, 16 μg of pDNA) were administered into nude mice by i.t. injection. The NIR imaging was obtained at different p.i. time points via a UVP ChemStudio PLUS 815 imaging system equipped with a 150 W Xe-lamp (Analytikjena, USA). All images were taken with long-pass emission filter (800 nm longer) and band-pass excitation filter of 600–645 nm. Data acquisition and analysis was performed using a VisionWorks 8.20.

4.6 *In vivo* metabolism and biodistribution

MDA-MB-231 tumor-bearing Balb/c nude mice were utilized to investigate the metabolism and biodistribution of the AuNPs@CP-pDNA. The AuNPs@CP-pDNA (80 μL, 1.3 μM of AuNPs, 16 μg of pDNA) was i.t. injected into the nude mice. After 72 h, the mice were sacrificed and the biological tissues (heart, liver, spleen, lung, kidney, skin, stomach, intestines, and tumor) and metabolites (urine and feces) were collected. The above samples were dissolved via fresh aqua regia (HCl/HNO_3 = 3:1, v/v), and digested with a maximum temperature of 120 °C until these mixed solutions were completely evaporated. Finally, all the experimental samples were measured by an ICP-MS system using Rhenium as internal standard.

4.7 Immunofluorescence staining

Immunofluorescence staining were used to evaluate the expression level of i.t. p53 protein. The above harvested tumors were fixed in 4% neutral buffered paraformaldehyde and embedded in paraffin. Tumor tissues were cryo-sectioned into slices at a thickness of ~ 10 μm. After incubation in BSA, sections were incubated with p53 antibody (Enogene, E1A6073, 1:100) mixture at 4 °C overnight, and the excess p53 antibody was removed in washing buffer. Afterwards, the tumor slices were incubated with secondary antibody conjugated with fluorescein isothiocyanate (FITC) (goat anti-rabbit; 1:200) at 37 °C for 1 h. Stained microscopic tumor slices were washed in washing buffer and demineralized water, and were then mounted with medium containing 4,6-diamidino-2-phenylindole (DAPI, Servicebio). All tumor slices were observed on a Nikon Ecliose C1 fluorescence microscope (Nikon, Japan) using appropriate filters. Image post-processing (intensity statistics and merging) was performed using both VisionWorks 8.20 and Case Viewer 2.0.

Acknowledgements

This work was supported by the National Natural Science Foundation of China (Nos. 21573078 and 22022403), Guangdong Natural Science Funds for Distinguished Young Scholars (No. 2016A030306024), Guangzhou Science and Technology Project (No. 201904010055), and Fundamental Research Funds for the Central Universities.

Electronic Supplementary Material: Supplementary material (materials and equipment, characterization of the self-assembled AuNPs@CP, cytotoxicity assay, cellular uptake, endocytosis inhibition assay, western blot analysis, and *in vivo* toxicity analysis) is available in the online version of this article at https://doi.org/10.1007/s12274-020-3153-6.

References

[1] Crawford, S. E.; Hartmann, M. J.; Millstone, J. E. Surface chemistry-mediated near-infrared emission of small coinage metal nanoparticles. *Acc. Chem. Res*. **2019**, *52*, 695–703.

[2] Wu, Z. N.; Du, Y. H.; Liu, J. L.; Yao, Q. F.; Chen, T. K.; Cao, Y. T.; Zhang, H.; Xie, J. P. Aurophilic interactions in the self-assembly of gold nanoclusters into nanoribbons with enhanced luminescence. *Angew. Chem., Int. Ed*. **2019**, *58*, 8139–8144.

[3] Gong, L. S.; Chen, Y.; He, K.; Liu, J. B. Surface coverage-regulated cellular interaction of ultrasmall luminescent gold nanoparticles. *ACS Nano* **2019**, *13*, 1893–1899.

[4] Zheng, K. Y.; Setyawati, M. I.; Leong, D. T.; Xie, J. P. Surface ligand chemistry of gold nanoclusters determines their antimicrobial ability. *Chem. Mater*. **2018**, *30*, 2800–2808.

[5] Yu, M. X.; Xu, J.; Zheng, J. Renal clearable luminescent gold nanoparticles: From the bench to the clinic. *Angew. Chem., Int. Ed*. **2019**, *58*, 4112–4128.

[6] Li, L.; Yang, Z.; Fan, W. P.; He, L. C.; Cui, C.; Zou, J. H.; Tang, W.; Jacobson, O.; Wang, Z. T.; Niu, G. et al. *In situ* polymerized hollow mesoporous organosilica biocatalysis nanoreactor for enhancing ROS-mediated anticancer therapy. *Adv. Funct. Mater*. **2020**, *30*, 1907716.

[7] Liao, L. W.; Zhuang, S. L.; Wang, P.; Xu, Y. N.; Yan, N.; Dong, H. W.; Wang, C. M.; Zhao, Y.; Xia, N.; Li, J. et al. Quasi-dual-packed-kerneled Au_{49}(2,4-DMBT)$_{27}$ nanoclusters and the influence of kernel packing on the electrochemical gap. *Angew. Chem., Int. Ed*. **2017**, *56*, 12644–12648.

[8] Chen, D. Y.; Luo, Z. T.; Li, N. J.; Lee, J. Y.; Xie, J. P.; Lu, J. M. Amphiphilic polymeric nanocarriers with luminescent gold nanoclusters for concurrent bioimaging and controlled drug release. *Adv. Funct. Mater*. **2013**, *23*, 4324–4331.

[9] Jiang, X. Y.; Du, B. J.; Zheng, J. Glutathione-mediated biotransformation in the liver modulates nanoparticle transport. *Nat. Nanotechnol*. **2019**, *14*, 874–882.

[10] Lei, Y. F.; Tang, L. X.; Xie, Y. Z. Y.; Xianyu, Y. L.; Zhang, L. M.; Wang, P.; Hamada, Y.; Jiang, K.; Zheng, W. F.; Jiang, X. Y. Gold nanoclusters-assisted delivery of *NGF* siRNA for effective treatment of pancreatic cancer. *Nat. Commun*. **2017**, *8*, 15130.

[11] Sun, Y. Q.; Wang, D. D.; Zhao, Y. Q.; Zhao, T. X.; Sun, H. C.; Li, X. W.; Wang, C. X.; Yang, B.; Lin, Q. Polycation-functionalized gold nanodots with tunable near-infrared fluorescence for simultaneous gene delivery and cell imaging. *Nano Res*. **2018**, *11*, 2392–2404.

[12] Li, Q. Z.; Pan, Y. T.; Chen, T. K.; Du, Y. X.; Ge, H. H.; Zhang, B. C.; Xie, J. P.; Yu, H. Z.; Zhu, M. Z. Design and mechanistic study of a novel gold nanocluster-based drug delivery system. *Nanoscale* **2018**, *10*, 10166–10172.

[13] Yahia-Ammar, A.; Sierra, D.; Mérola, F.; Hildebrandt, N.; Le Guével, X. Self-assembled gold nanoclusters for bright fluorescence imaging and enhanced drug delivery. *ACS Nano* **2016**, *10*, 2591–2599.

[14] Gilleron, J.; Querbes, W.; Zeigerer, A.; Borodovsky, A.; Marsico, G.; Schubert, U.; Manygoats, K.; Seifert, S.; Andree, C.; Stöter, M. et al. Image-based analysis of lipid nanoparticle–mediated siRNA delivery, intracellular trafficking and endosomal escape. *Nat. Biotechnol*. **2013**, *31*, 638–646.

[15] Wang, P. F.; Rahman, M. A.; Zhao, Z. X.; Weiss, K.; Zhang, C.; Chen, Z. J.; Hurwitz, S. J.; Chen, Z. G.; Shin, D. M.; Ke, Y. G. Visualization of the cellular uptake and trafficking of DNA origami nanostructures in cancer cells. *J. Am. Chem. Soc*. **2018**, *140*, 2478–2484.

[16] Qi, G. B.; Gao, Y. J.; Wang, L.; Wang, H. Self-assembled peptide-based nanomaterials for biomedical imaging and therapy. *Adv. Mater*. **2018**, *30*, 1703444.

[17] Sato, K.; Hendricks, M. P.; Palmer, L. C.; Stupp, S. I. Peptide supramolecular materials for therapeutics. *Chem. Soc. Rev*. **2018**, *47*, 7539–7551.

[18] Li, M.; Ehlers, M.; Schlesiger, S.; Zellermann, E.; Knauer, S. K.; Schmuck, C. Incorporation of a non-natural arginine analogue into a cyclic peptide leads to formation of positively charged nanofibers capable of gene transfection. *Angew. Chem., Int. Ed*. **2016**, *55*, 598–601.

[19] Zhang, W. S.; Lin, D. M.; Wang, H. X.; Li, J. F.; Nienhaus, G. U.; Su, Z. Q.; Wei, G.; Shang, L. Supramolecular self-assembly bioinspired synthesis of luminescent gold nanocluster-embedded peptide nanofibers for temperature sensing and cellular imaging. *Bioconjugate Chem*. **2017**, *28*, 2224–2229.

[20] Fan, Z.; Sun, L. M.; Huang, Y. J.; Wang, Y. Z.; Zhang, M. J. Bioinspired fluorescent dipeptide nanoparticles for targeted cancer cell imaging and real-time monitoring of drug release. *Nat. Nanotechnol*. **2016**, *11*, 388–394.

[21] Wang, Y.; Lin, Y. X.; Qiao, Z. Y.; An, H. W.; Qiao, S. L.; Wang, L.; Rajapaksha, R. P. Y. J.; Wang, H. Self-assembled autophagy-inducing polymeric nanoparticles for breast cancer interference *in-vivo*. *Adv. Mater*. **2015**, *27*, 2627–2634.

[22] Fan, Z.; Chang, Y.; Cui, C. C.; Sun, L. M.; Wang, D. H.; Pan, Z.; Zhang, M. J. Near infrared fluorescent peptide nanoparticles for enhancing esophageal cancer therapeutic efficacy. *Nat. Commun*. **2018**, *9*, 2605.

[23] Pugliese, R.; Marchini, A.; Saracino, G. A. A.; Zuckermann, R. N.; Gelain, F. Cross-linked self-assembling peptide scaffolds. *Nano Res*. **2018**, *11*, 586–602.
[24] Liu, J. B.; Yu, M. X.; Zhou, C.; Yang, S. Y.; Ning, X. H.; Zheng, J. Passive tumor targeting of renal-clearable luminescent gold nanoparticles: Long tumor retention and fast normal tissue clearance. *J. Am. Chem. Soc*. **2013**, *135*, 4978–4981.
[25] Liu, J. B.; Duchesne, P. N.; Yu, M. X.; Jiang, X. Y.; Ning, X. H.; Vinluan III, R. D.; Zhang, P.; Zheng, J. Luminescent gold nanoparticles with size-independent emission. *Angew. Chem., Int. Ed*. **2016**, *55*, 8894–8898.
[26] Ghadiri, M. R.; Granja, J. R.; Milligan, R. A.; McRee, D. E.; Khazanovich, N. Self-assembling organic nanotubes based on a cyclic peptide architecture. *Nature* **1993**, *366*, 324–327.
[27] Lamas, A.; Guerra, A.; Amorín, M.; Granja, J. R. New self-assembling peptide nanotubes of large diameter using δ-amino acids. *Chem. Sci*. **2018**, *9*, 8228–8233.
[28] Zhou, T. Y.; Zhu, J. Y.; Gong, L. S.; Nong, L. T.; Liu, J. B. Amphiphilic block copolymer-guided *in situ* fabrication of stable and highly controlled luminescent copper nanoassemblies. *J. Am. Chem. Soc*. **2019**, *141*, 2852–2856.
[29] Ling, D. S.; Hackett, M. J.; Hyeon, T. Surface ligands in synthesis, modification, assembly and biomedical applications of nanoparticles. *Nano Today* **2014**, *9*, 457–477.
[30] Chithrani, B. D.; Chan, W. C. W. Elucidating the mechanism of cellular uptake and removal of protein-coated gold nanoparticles of different sizes and shapes. *Nano Lett*. **2007**, *7*, 1542–1550.
[31] Lu, J. X.; Wang, J.; Ling, D. S. Surface engineering of nanoparticles for targeted delivery to hepatocellular carcinoma. *Small* **2018**, *14*, 1702037.
[32] Wu, X. A.; Choi, C. H. J.; Zhang, C.; Hao, L. L.; Mirkin, C. A. Intracellular fate of spherical nucleic acid nanoparticle conjugates. *J. Am. Chem. Soc*. **2014**, *136*, 7726–7733.
[33] Vindigni, G.; Raniolo, S.; Ottaviani, A.; Falconi, M.; Franch, O.; Knudsen, B. R.; Desideri, A.; Biocca, S. Receptor-mediated entry of pristine octahedral DNA nanocages in mammalian cells. *ACS Nano* **2016**, *10*, 5971–5979.
[34] Zinchuk, V.; Zinchuk, O.; Okada, T. Quantitative colocalization analysis of multicolor confocal immunofluorescence microscopy images: Pushing pixels to explore biological phenomena. *Acta Histochem. Cytochem*. **2007**, *40*, 101–111.
[35] Zhu, J. Y.; He, K.; Dai, Z. Y.; Gong, L. S.; Zhou, T. Y.; Liang, H. R.; Liu, J. B. Self-assembly of luminescent gold nanoparticles with sensitive pH-stimulated structure transformation and emission response toward lysosome escape and intracellular imaging. *Anal. Chem*. **2019**, *91*, 8237–8243.
[36] Iversen, T. G.; Skotland, T.; Sandvig, K. Endocytosis and intracellular transport of nanoparticles: Present knowledge and need for future studies. *Nano Today* **2011**, *6*, 176–185.
[37] Huang, J.; Zong, C.; Shen, H.; Liu, M.; Chen, B.; Ren, B.; Zhang, Z. J. Mechanism of cellular uptake of graphene oxide studied by surface-enhanced Raman spectroscopy. *Small* **2012**, *8*, 2577–2584.
[38] Akishiba, M.; Takeuchi, T.; Kawaguchi, Y.; Sakamoto, K.; Yu, H. H.; Nakase, I.; Takatani-Nakase, T.; Madani, F.; Gräslund, A.; Futaki, S. Cytosolic antibody delivery by lipid-sensitive endosomolytic peptide. *Nat. Chem*. **2017**, *9*, 751–761.
[39] Gratton, S. E. A.; Ropp, P. A.; Pohlhaus, P. D.; Luft, J. C.; Madden, V. J.; Napier, M. E.; DeSimone, J. M. The effect of particle design on cellular internalization pathways. *Proc. Natl. Acad. Sci. USA* **2008**, *105*, 11613–11618.
[40] Jana, P.; Samanta, K.; Bäcker, S.; Zellermann, E.; Knauer, S.; Schmuck, C. Efficient gene transfection through inhibition of β-sheet (amyloid fiber) formation of a short amphiphilic peptide by gold nanoparticles. *Angew. Chem., Int. Ed*. **2017**, *56*, 8083–8088.
[41] Liu, Y. H.; Zhang, X. N.; Han, C.; Wan, G. H.; Huang, X. X.; Ivan, C.; Jiang, D. H.; Rodriguez-Aguayo, C.; Lopez-Berestein, G.; Rao, P. H. et al. TP53 loss creates therapeutic vulnerability in colorectal cancer. *Nature* **2015**, *520*, 697–701.
[42] Bykov, V. J. N.; Eriksson, S. E.; Bianchi, J.; Wiman, K. G. Targeting mutant p53 for efficient cancer therapy. *Nat. Rev. Cancer* **2017**, *18*, 89–102.
[43] Capasso Palmiero, U.; Kaczmarek, J. C.; Fenton, O. S.; Anderson, D. G. Poly(β-amino ester)-*co*-poly(caprolactone) terpolymers as nonviral vectors for mRNA delivery *in vitro* and *in vivo*. *Adv. Healthcare Mater*. **2018**, *7*, 1800249.
[44] Takagi, M.; Absalon, M. J.; McLure, K. G.; Kastan, M. B. Regulation of p53 translation and induction after DNA damage by ribosomal protein L26 and nucleolin. *Cell* **2005**, *123*, 49–63.
[45] Kubbutat, M. H. G.; Jones, S. N.; Vousden, K. H. Regulation of p53 stability by Mdm2. *Nature* **1997**, *387*, 299–303.
[46] Chen, Q.; Wang, C.; Zhang, X. D.; Chen, G. J.; Hu, Q. Y.; Li, H. J.; Wang, J. Q.; Wen, D.; Zhang, Y. Q.; Lu, Y. F. et al. *In situ* sprayed bioresponsive immunotherapeutic gel for post-surgical cancer treatment. *Nat. Nanotechnol*. **2019**, *14*, 89–97.